PHYSICAL REVIEW D **96,** 075045 (2017)

Gravitational waves from hidden QCD phase transition

Mayumi Aoki,[*] Hiromitsu Goto,[†] and Jisuke Kubo[‡]

Institute for Theoretical Physics, Kanazawa University, Kanazawa 920-1192, Japan

(Received 29 September 2017; published 31 October 2017)

Drastic changes in the early Universe such as first-order phase transition can produce a stochastic gravitational wave (GW) background. We investigate the testability of a scale invariant extension of the standard model (SM) using the GW background produced by the chiral phase transition in a strongly interacting QCD-like hidden sector, which, via a SM singlet real scalar mediator, triggers the electroweak phase transition. Using the Nambu–Jona-Lasinio method in a mean field approximation we estimate the GW signal and find that it can be tested by future space-based detectors.

DOI: 10.1103/PhysRevD.96.075045

I. INTRODUCTION

It is a challenge for physics beyond the standard model (SM) to answer a long-standing question—what is the origin of mass? The same question applies to dark matter (DM), which, if it is a particle, is absent in the SM. Though various suggestions about how to go beyond the SM exist, there is so far no sign for that from the Large Hadron Collider (LHC) experiments [1,2] and no sign from the current DM detection experiments either [3,4].

In contrast to this situation, the first observation of the gravitational wave (GW) signal at LIGO [5] has opened up a new way to study astrophysical phenomena and has awakened the hope in particle cosmology that phenomena in the early Universe can also be probed by the GW. It has indeed been known that phenomena in the early Universe such as inflation [6], topological defects [7], and first-order phase transition [8] generate a non-localized stochastic GW background. In particular, phase transitions in particle physics are associated with symmetry breaking, and therefore the GW signals produced by these phase transitions can be an alternative approach to investigate the structure of symmetries in the early Universe. Unfortunately, because of not being first order, the phase transition associated with the electroweak (EW) symmetry breaking in the SM cannot produce the GW background [9–11]. However, if the SM is extended, observable GW signals associated with a symmetry breaking may be produced and tested in future experiments such as LISA [12,13] and DECIGO [14–16], as discussed in [17–33].

As lattice simulations in QCD have shown [34–36], the chiral phase transition in QCD is, due to a relatively large current mass of the strange quark, a crossover type. This does not prevent the possibility that the chiral phase transition in a QCD-like hidden sector is of first order.[1] In fact, such a possibility with a critical temperature of $\mathcal{O}(1)$ TeV has been recently found [42,43] in a scale invariant extension of the SM [42–48], in which dynamical chiral symmetry breaking (DχSB) in a QCD-like hidden sector triggers the EW symmetry breaking. In the present paper we focus on this model. In this model, moreover, the EW energy scale and the DM mass have the same origin. In most of the parameter space, the DM mass is created before the EW phase transition and, in a certain region of the parameter space, it takes place during a strong first-order chiral phase transition. By choosing various benchmark points in the parameter space we study the testability of the GW background produced by this phase transition.

The paper is organized as follows. In Sec. II we briefly review the scale invariant extension of the SM with a QCD-like hidden sector and describe how we use the Nambu–Jona-Lasinio (NJL) model [49–51] as an effective low-energy theory in a mean field approximation [52,53]. We fix the number of the hidden color n_c and flavor n_f both at 3, because we can simply rescale the values of the NJL parameters for the real hadrons. In this way we can avoid increasing the number of independent parameters when going from the high-energy theory to the low-energy effective theory. We pick up a set of four benchmark parameters, for which the chiral phase transition in the hidden QCD sector is of first order. For these points we calculate the GW signals.

Note that the chiral phase transition in our model occurs in a two-dimensional parameter space, the chiral condensate and the vacuum expectation value (VEV) of the SM singlet real scalar (which is the mediator of the energy scale from the hidden sector to the SM sector). Furthermore, the mean field σ corresponding to the chiral condensate is a

[*]mayumi@hep.s.kanazawa-u.ac.jp
[†]goto@hep.s.kanazawa-u.ac.jp
[‡]jik@hep.s.kanazawa-u.ac.jp

[1]Other possibilities of a first-order phase transition in a QCD-like theory are the deconfinement/confinement phase transition in the quenched QCD [35] and the chiral phase transition in QCD with a large baryon chemical potential [37,38]. They may produce the observable GW signal as discussed in [39–41].

nonpropagating field at the zeroth order in the mean field approximation: It becomes a quantum field at the one-loop level, so that its wave function renormalization constant is far from 1 and depends on the mean fields as well as on the temperature. In Sec. III we discuss how to manage the complications mentioned above to compute the rate of the bubble nucleation that occurs during the cosmological tunneling in the hidden QCD sector. In Sec. IV we discuss the detectability of the GW signals produced by the chiral phase transition for the benchmark points in the parameter space. We summarize and conclude in Sec. V.

II. THE MODEL

We consider a classically scale invariant extension of the SM studied in [42–46], which consists of a hidden $\mathrm{SU}(n_c)_{\mathrm{H}}$ gauge sector coupled via a real singlet scalar field S to the SM. The Lagrangian of the hidden sector is written as

$$\mathcal{L}_{\mathrm{H}} = -\frac{1}{2}\mathrm{Tr}F^2 + \mathrm{Tr}\bar{\psi}(i\not{D} - yS)\psi, \tag{1}$$

where the hidden vectorlike fermions $\psi_i (i = 1, \ldots, n_f)$ transform as a fundamental representation of $\mathrm{SU}(n_c)_{\mathrm{H}}$. The $\mathcal{L}_{\mathrm{SM}+S}$ part of the total Lagrangian $\mathcal{L}_{\mathrm{T}} = \mathcal{L}_{\mathrm{SM}+S} + \mathcal{L}_{\mathrm{H}}$ contains the SM gauge and Yukawa interactions along with the scalar potential

$$V_{\mathrm{SM}+S} = \lambda_H (H^\dagger H)^2 + \frac{1}{4}\lambda_S S^4 - \frac{1}{2}\lambda_{HS} S^2 (H^\dagger H), \tag{2}$$

where $H^T = (H^+, (h+G)/\sqrt{2})$ is the SM Higgs doublet field with H^+ and G as the would-be Nambu-Goldstone (NG) fields. The scalar couplings at the tree level have to satisfy the stability condition for the scalar potential

$$\lambda_H > 0, \quad \lambda_S > 0 \quad \text{and} \quad 2\sqrt{\lambda_H \lambda_S} - \lambda_{HS} > 0. \tag{3}$$

Here y and λ_{HS} are assumed to be positive. This model explains the origin of the mass of the Higgs boson and the DM in the following sense.

(i) First, due to the DχSB in the hidden sector, a nonzero chiral condensate $\langle\bar{\psi}\psi\rangle$ forms and generates a mass scale above the EW scale. Consequently, NG bosons, which are mesons in the hidden sector, appear.

(ii) At the same time of the hidden DχSB, the singlet scalar field S acquires a nonzero VEV$\langle S\rangle$ because of the Yukawa interaction $-yS\bar{\psi}\psi$. Note that the Yukawa interaction breaks the chiral symmetry explicitly, and $y\langle S\rangle$ plays the role of a current mass. Therefore, the mass of the hidden mesons depends crucially on $y\langle S\rangle$.

(iii) These hidden mesons (or a part of them) can become DM candidates, because they are stable due to the vectorlike flavor symmetry that is left unbroken after the DχSB.

(iv) The EW symmetry breaking is triggered by the Higgs mass term that is nothing but the scalar coupling $+\frac{1}{2}\lambda_{HS}S^2H^\dagger H$ with the nonzero $\langle S\rangle$.

In this work we consider the case with $n_c = n_f = 3$ and assume that the singlet scalar S equally couples to the hidden fermions. Then the hidden chiral symmetry $\mathrm{SU}(3)_L \times \mathrm{SU}(3)_R$ is dynamically broken down to $\mathrm{SU}(3)_V$, and thanks to this unbroken symmetry, eight hidden pions become a DM candidate. The DM physics and the impact of the hidden chiral phase transition to the EW phase transition have been investigated in [42] by using the NJL theory [49–51] in the self-consistent mean field (SCMF) approximation [52,53]. It has been found that a strong first-order chiral phase transition can occur if the Yukawa coupling y is small enough, i.e., $y \lesssim 0.006$ [43]. Within the framework of the NJL theory we will calculate the GW spectrum produced by the hidden chiral phase transition later on. The same model has been analyzed by using a linear [44] and nonlinear [45] sigma model and also AdS/QCD approach [48]. In [54], the GW spectrum from the hidden chiral phase transition has been calculated within the framework of a linear sigma model.

A. Nambu–Jona-Lasinio Lagrangian in a mean field approximation

Following [42] we approximate the high-energy Lagrangian (1) by the NJL Lagrangian

$$\mathcal{L}_{\mathrm{NJL}} = \mathrm{Tr}\bar{\psi}(i\not{\partial} - yS)\psi + 2G\mathrm{Tr}\Phi^\dagger\Phi + G_D(\det\Phi + \mathrm{H.c.}), \tag{4}$$

where G and G_D are dimensional parameters and

$$(\Phi)_{ij} = \bar{\psi}_i(1-\gamma_5)\psi_j = \frac{1}{2}\lambda^a_{ji}\mathrm{Tr}\bar{\psi}\lambda^a(1-\gamma_5)\psi,$$
$$(\Phi^\dagger)_{ij} = \bar{\psi}_i(1+\gamma_5)\psi_j = \frac{1}{2}\lambda^a_{ji}\mathrm{Tr}\bar{\psi}\lambda^a(1+\gamma_5)\psi.$$

Here $\lambda^a (a = 1, \ldots, 8)$ are the Gell-Mann matrices with $\lambda^0 = \sqrt{2/3}$. To deal with the NJL Lagrangian (4), which is nonrenormalizable, we work in the SCMF approximation [52,53]. The mean fields σ and ϕ_a are defined in the "Bardeen-Cooper-Schrieffer" vacuum as

$$\langle\Phi\rangle = -\frac{1}{4G}(\mathrm{diag}(\sigma,\sigma,\sigma) + i(\lambda^a)^T\phi_a). \tag{5}$$

After splitting up the NJL Lagrangian into the sum $\mathcal{L}_{\mathrm{NJL}} = \mathcal{L}_{\mathrm{MFA}} + \mathcal{L}_I$, where $\mathcal{L}_{\mathrm{MFA}}$ contains at most bilinear terms of ψ_i and $\mathcal{L}_I$ is normal ordered with respect to the Bardeen-Cooper-Schrieffer vacuum, we find the Lagrangian in the SCMF approximation:

$$\mathcal{L}_{\rm MFA} = {\rm Tr}\bar{\psi}(i\bar{\partial} - M)\psi - i{\rm Tr}\bar{\psi}\gamma_5\phi\psi - \frac{1}{8G}\left(3\sigma^2 + 2\sum_{a=1}^{8}\phi_a\phi_a\right) + \frac{G_D}{8G^2}\left(-{\rm Tr}\bar{\psi}\phi^2\psi + \sum_{a=1}^{8}\phi_a\phi_a{\rm Tr}\bar{\psi}\psi + i\sigma{\rm Tr}\bar{\psi}\gamma_5\phi\psi + \frac{\sigma^3}{2G} + \frac{\sigma}{2G}\sum_{a=1}^{8}(\phi_a)^2\right), \quad (6)$$

where $\phi = \sum_{a=1}^{8}\phi_a\lambda^a$, we have suppressed ϕ_0 here, and M is given by

$$M = \sigma + yS - \frac{G_D}{8G^2}\sigma^2. \quad (7)$$

Through integrating out the hidden fermions, a nontrivial correction to the tree-level potential for σ is generated, such that the position of the potential minimum can be shifted from zero to a finite value of σ. From the definition (5) we see that this is nothing but the chiral condensate in the SCMF approximation. By self-consistency it is meant that the actual value of $\langle\sigma\rangle$ is computed afterward at the loop level, and then we consider the mean field Lagrangian (6) around this mean field vacuum. At the tree level of (6), the mean fields σ and ϕ_a are nonpropagating classical fields. Through integrating out the hidden fermions at the one-loop level, their kinetic terms are also generated. At this stage we reinterpret them as propagating quantum fields.

B. Mass spectrum

The chiral condensation in the hidden sector can be studied by using the one-loop effective potential obtained from the mean field Lagrangian (6):

$$V_{\rm eff} = V_{\rm SM+S} + V_{\rm NJL}, \quad (8)$$

where

$$V_{\rm NJL}(\sigma, S; \Lambda_{\rm H}) = \frac{3}{8G}\sigma^2 - \frac{G_D}{16G^3}\sigma^3 - 3n_c I_0(M; \Lambda_{\rm H}), \quad (9)$$

and I_0 is given by

$$I_0(M;\Lambda) = \frac{1}{16\pi^2}\left[\Lambda^4\ln\left(1+\frac{M^2}{\Lambda^2}\right) - M^4\ln\left(1+\frac{\Lambda^2}{M^2}\right) + \Lambda^2M^2\right]. \quad (10)$$

Here we have used the four-dimensional cutoff, and Λ is the corresponding cutoff parameter. The NJL parameters for the hidden QCD are obtained by scaling up the values of G, G_D, and Λ for the real hadrons. That is, we assume that the dimensionless combinations

$$G^{1/2}\Lambda = 1.82, \qquad (-G_D)^{1/5}\Lambda = 2.29, \quad (11)$$

which are satisfied for the real hadrons, remain unchanged for a higher scale of Λ. For a given set of the free parameters of the model λ_H, λ_{HS}, λ_S, and y, the VEV of σ and S can be determined through the minimization of the scalar potential $V_{\rm eff}(h, S, \sigma; \Lambda_{\rm H})$, where the hidden QCD scale $\Lambda_{\rm H}$ is so chosen to satisfy $\langle h\rangle = 246$ GeV.

The mass spectrum of the particles can be computed from the corresponding two-point functions, which are obtained by integrating out the hidden fermions. Note that the CP-even scalars h, S, and σ mix with one another. The flavor eigenstates $\varphi_i (i = h, S, \sigma)$ and the mass eigenstates $s_i (i = 1, 2, 3)$ are related by $\varphi_i = \xi_i^{(j)} s_j$. Their masses are determined by the zeros of the two-point functions $\Gamma_{ij}(i, j = h, S, \sigma)$ at the one-loop level, i.e., $\Gamma_{ij}(m_k^2)\xi_j^{(k)} = 0$, where

$$\begin{aligned}
\Gamma_{hh}(p^2) &= p^2 - 3\lambda_H\langle h\rangle^2 + \frac{1}{2}\lambda_{HS}\langle S\rangle^2,\\
\Gamma_{hS} &= \lambda_{HS}\langle h\rangle\langle S\rangle, \qquad \Gamma_{h\sigma} = 0,\\
\Gamma_{SS}(p^2) &= p^2 - 3\lambda_S\langle S\rangle^2 + \frac{1}{2}\lambda_{HS}\langle h\rangle^2 - y^2 3n_c I_{\varphi^2}(p^2, M; \Lambda_{\rm H}),\\
\Gamma_{S\sigma}(p^2) &= -y\left(1 - \frac{G_D\langle\sigma\rangle}{4G^2}\right)3n_c I_{\varphi^2}(p^2, M; \Lambda_{\rm H}),\\
\Gamma_{\sigma\sigma}(p^2) &= -\frac{3}{4G} + \frac{3G_D\langle\sigma\rangle}{8G^3} - \left(1 - \frac{G_D\langle\sigma\rangle}{4G^2}\right)^2 3n_c I_{\varphi^2}(p^2, M; \Lambda_{\rm H}) + \frac{G_D}{G^2}3n_c I_V(M; \Lambda_{\rm H}),
\end{aligned} \quad (12)$$

and the loop functions are defined as

$$I_{\varphi^2}(p^2, M; \Lambda) = \int_\Lambda \frac{d^4k}{i(2\pi)^4}\frac{{\rm Tr}(\not{k} + \not{p} + M)(\not{k} + M)}{((k+p)^2 - M^2)(k^2 - M^2)}, \quad (13)$$

$$I_V(M;\Lambda) = \int_\Lambda \frac{d^4k}{i(2\pi)^4}\frac{M}{(k^2 - M^2)} = -\frac{1}{16\pi^2}M\left[\Lambda^2 - M^2\ln\left(1+\frac{\Lambda^2}{M^2}\right)\right]. \quad (14)$$

We identify the SM Higgs with the mass eigenstate corresponding to ξ_1, which is supposed to be closest to (1,0,0), and its mass is $m_1 = m_h = 125.09 \pm 0.24$ GeV [55]. Similarly we use $m_2 = m_S$ and $m_3 = m_\sigma$. The DM candidate is the hidden pion ϕ_a and its mass is also generated at the one-loop level. Its two-point function is

$$\Gamma_{\rm DM}(p^2) = -\frac{1}{2G} + \frac{G_D\langle\sigma\rangle}{8G^3} + \left(1 - \frac{G_D\langle\sigma\rangle}{8G^2}\right)^2 2n_c I_{\phi^2}(p^2, M; \Lambda_{\rm H}) + \frac{G_D}{G^2} n_c I_V(M; \Lambda_{\rm H}), \tag{15}$$

where the loop function is given by

$$I_{\phi^2}(p^2, M; \Lambda) = \int_\Lambda \frac{d^4k}{i(2\pi)^4} \frac{{\rm Tr}(\not{k} - \not{p} + M)\gamma_5(\not{k} + M)\gamma_5}{((k-p)^2 - M^2)(k^2 - M^2)}. \tag{16}$$

Then we can calculate the DM mass from $\Gamma_{\rm DM}(m_{\rm DM}^2) = 0$.

Once the set of the parameters $(\lambda_H, \lambda_{HS}, \lambda_S, y)$ is given, the mass spectrum of the hidden sector particles is fixed. Figure 1 shows the Yukawa coupling y dependence of the masses $m_{\rm DM}$ (left) and of the hidden QCD scale $\Lambda_{\rm H}$ (right) for $\lambda_H = 0.13$, $\lambda_S = 0.08$ with two different values of λ_{HS}; $\lambda_{HS} = 0.001$ (solid lines) and 0.002 (dashed lines). As shown in Fig. 1 (left), the DM mass $m_{\rm DM}$ is proportional to the Yukawa coupling y. This is because the Yukawa interaction breaks the chiral symmetry explicitly. The scale of the DχSB in the hidden sector, which is the hidden QCD scale $\Lambda_{\rm H}$, depends on how the mediator S transfers the mass scale to the SM sector. The larger the couplings λ_{HS} and y are, the closer to the EW scale the hidden QCD scale $\Lambda_{\rm H}$ is located as seen in Fig. 1 (right). Moreover, the annihilation processes of the DM also depend on the mass spectrum and the Yukawa coupling y. Note that the one-loop effective couplings are given by $\Gamma_{\phi\phi S} \propto y$ and $\Gamma_{\phi\phi SS} \propto y^2$. In the small y area with $m_S > m_{\rm DM}$, the mass spectrum should satisfy the resonance condition $m_S \simeq 2m_{\rm DM}$ to obtain a realistic DM relic abundance and, in this parameter space, the spin-independent cross section of DM off the nucleon becomes so small [42] that it will be very difficult to detect DM at direct DM detection experiments such as XENON1T [4]. On the other hand, the GW signal might be observed since a strong first-order chiral phase transition can appear for a small y area [43].

C. Chiral phase transitions

The phase transition at finite temperature can be studied using a one-loop effective potential. Since the EW phase transition occurs well below the critical temperature of the chiral phase transition in the hidden sector, we may assume $\langle h\rangle = 0$ in investigating the chiral phase transition. Accordingly, the scalar potential to be analyzed is

$$V_{\rm EFF}(S, \sigma, T) = V^{h\to 0}_{\rm SM+S}(S) + V_{\rm NJL}(S, \sigma) + V_{\rm CW}(S) + V_{\rm FT}(S, \sigma, T) + V_{\rm RING}(S, T), \tag{17}$$

where $V_{\rm SM+S}$ and $V_{\rm NJL}$ are given, respectively, in (2) and (9),

$$V_{\rm CW}(S) = -\frac{9}{4}\frac{\lambda_S^2}{32\pi^2}(S^4 - \langle S\rangle^4) + \frac{m_S^4(S)}{64\pi^2}\ln\left[\frac{m_S^2(S)}{m_S^2(\langle S\rangle)}\right], \tag{18}$$

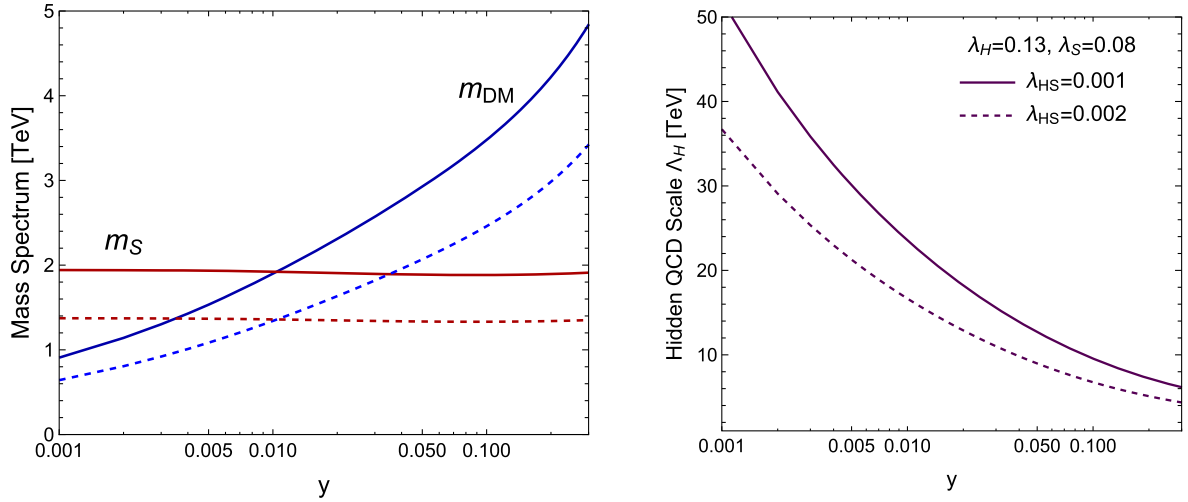

FIG. 1. The masses $m_{\rm DM}$ (left) and the hidden QCD scale $\Lambda_{\rm H}$ (right) versus y for $\lambda_H = 0.13$, $\lambda_S = 0.08$ with two different values of λ_{HS}; $\lambda_{HS} = 0.001$ (solid lines) and 0.002 (dashed lines)

$$V_{\rm FT}(S,\sigma,T) = \frac{T^4}{2\pi^2} J_B(m_S^2(S)/T^2) - 6n_c \frac{T^4}{\pi^2} J_F(M^2(S,\sigma)/T^2), \quad (19)$$

$$V_{\rm RING}(S,T) = -\frac{T}{12\pi}[(M_S^2(S,T))^{3/2} - (m_S^2(S))^{3/2}], \quad (20)$$

and $m_S^2(S) = 3\lambda_S S^2 + \mathcal{O}(y^2)$ is the field-dependent mass for S with its thermal mass

$$M_S^2 = m_S^2(S) + \left(\frac{\lambda_S}{4} - \frac{\lambda_{HS}}{6}\right) T^2. \quad (21)$$

The thermal function is

$$J_{B,F}(r^2) = \int_0^\infty dx x^2 \ln(1 \mp e^{-\sqrt{x^2+r^2}}), \quad (22)$$

for which we use the approximate expression:

$$J_{B,F}(r^2) = e^{-r^2} \sum_{n=0}^{40} c_n^{B,F} r^{2n}. \quad (23)$$

D. Benchmark points

As discussed in [43], the chiral phase transition in the hidden sector becomes first order for small $y \lesssim 0.006$. We require the perturbativity and stability condition (3) of the scalar potential for $y \lesssim 0.006$ to be satisfied up to the Planck scale at the one-loop level.[2] We find that

$$0.13 \lesssim \lambda_H \lesssim 0.14, \qquad 0 < \lambda_{HS} < 0.12, \qquad 4\lambda_{HS}^2/\lambda_H < \lambda_S \lesssim 0.23 \quad (24)$$

should be satisfied to meet the requirements. The inequality $0 < \lambda_{HS}$ is our assumption [see (3)], and the interval of λ_H is due to the observed Higgs mass. The upper limit of λ_S comes from perturbativity, while the lower limit comes from the stability condition with finite λ_H and λ_{HS}. Note that there is no lower limit on λ_{HS} and y. We however consider only the case for $\lambda_{HS}, y \gtrsim 10^{-4}$, which implies that $\Lambda_{\rm H} < 200$ TeV.[3]

In Fig. 2 we show the area in the $m_{\rm DM}$–$\Lambda_{\rm H}$ plane, in which we obtain the VEV of the Higgs field $\langle h \rangle = 246$ GeV, the correct Higgs mass $m_h = 125.09 \pm 0.24$ GeV [55], h-S mixing $\xi_1^{(1)} > 0.99$ [55], and the resonance condition $m_S \simeq 2m_{\rm DM}$ (to realize the correct DM relic abundance). Note that the mass of the mediator S is bounded, because λ_S is bounded as discussed above. Consequently, because of the resonance condition $m_S \simeq 2m_{\rm DM}$, the DM mass is bounded, too. Similarly, $\Lambda_{\rm H}$ is bounded, because λ_{HS} is bounded from above (24) and from below due to our parameter choice $\lambda_{HS} > 10^{-4}$. The colored points A, B, C, and D in Fig. 2 are our benchmark points.

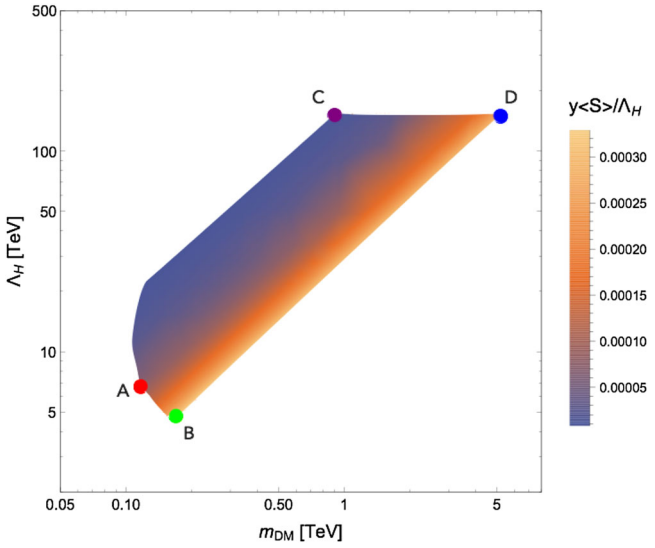

FIG. 2. The hidden QCD scale $\Lambda_{\rm H}$ against the DM mass $m_{\rm DM}$. In the colored region, $\langle h \rangle = 246$ GeV, $m_h = 125.09 \pm 0.24$ GeV, $\xi_1^{(1)} > 0.99$ ($h - S$ mixing), $m_S \simeq 2m_{\rm DM}$, and the perturbativity and stability constraint (24) are satisfied. We assumed the case for $\lambda_{HS}, y \gtrsim 10^{-4}$. The color strength indicates the value of $y\langle S \rangle/\Lambda_{\rm H}$, which is a measure of how the chiral symmetry is explicitly broken. The colored points are the benchmark points; the Cases A (red), B (green), C (purple), and D (blue) are defined in Table I.

The chosen four benchmark points are named Case A, B, C, and D: the set of the input parameter values $(\lambda_H, \lambda_{HS}, \lambda_S, y)$, along with the output values of $m_{\rm DM}$, $\Lambda_{\rm H}$, and $y\langle S \rangle/\Lambda_{\rm H}$ for each benchmark case, is given in Table I. Under $y \lesssim 0.006$ and (24), Cases A and B are located as close to the EW scale as possible and for C and D in an opposite way.[4] We regard the normalized current quark mass $y\langle S \rangle/\Lambda_{\rm H}$ as the characterization for the explicit chiral symmetry breaking. Their values should be compared with that of QCD, i.e., $m_u/\Lambda_{\rm QCD} \sim 6 \times 10^{-3}$ (in the NJL model).

In Fig. 3 we show the temperature dependence of $\langle \sigma \rangle/T$ and $\langle S \rangle/T$ near the critical temperature for each benchmark point. It can be seen that a first-order phase transition appears in all the cases. We also see that σ and S undergo the phase transition at the same time. Moreover, the phase

[2] According to [56], the hierarchy problem can be avoided in this way at least at the one-loop level.

[3] A large $\Lambda_{\rm H}$, which is realized by the small couplings y and λ_{HS}, does not necessarily mean a heavy S as shown in Fig. 1. Therefore, even if $\Lambda_{\rm H}$ is large, the correction to the Higgs mass coming from the internal S loop can be small.

[4] There exists the Higgs threshold between Cases A and B, which means the decay channel of the mediator S to two Higgs particles is forbidden only for Case A. This might become a benchmark point for a future collider search.

TABLE I. Four benchmark points, Cases A–D, which are defined by the values of $(\lambda_H, \lambda_{HS}, \lambda_S, y)$, where $m_{\rm DM}$, $\Lambda_{\rm H}$, and $y\langle S\rangle/\Lambda_{\rm H}$ are displayed for each case.

Case	$(\lambda_H, \lambda_{HS}, \lambda_S, y)$	$m_{\rm DM}$ (TeV)	$\Lambda_{\rm H}$ (TeV)	$y\langle S\rangle/\Lambda_{\rm H}$
A	$(0.140, 0.050, 0.054, 8.57\times10^{-4})$	0.117	6.84	7.30×10^{-6}
B	$(0.138, 0.098, 0.230, 3.60\times10^{-3})$	0.170	4.87	3.05×10^{-5}
C	$(0.129, 0.0001, 0.007, 1.07\times10^{-4})$	0.906	153.1	8.73×10^{-6}
D	$(0.130, 0.0001, 0.230, 3.55\times10^{-3})$	5.20	152.5	2.90×10^{-5}

transition in Case C appears for a slightly lower temperature compared with D even though $\Lambda_{\rm H}^{\rm C} > \Lambda_{\rm H}^{\rm D}$. The reason is that the explicit chiral symmetry breaking, whose strength is expressed by $y\langle S\rangle/\Lambda_{\rm H}$, influences not only the mass of DM but also the critical temperature. Since the chiral phase transition in the hidden sector occurs in the two-dimensional space (S, σ), we need to deal with quantum tunneling in the two-dimensional space to calculate the GW spectrum.

III. BUBBLES FROM HIDDEN QCD TUNNELING

Cosmological tunneling has been studied in [57–59]. The probability of the bubble nucleation per unit volume per unit time is given by

$$\Gamma = A(t)\exp\left[-S_E(t)\right], \tag{25}$$

where S_E is the Euclidean action. At a high temperature, the Euclidean action can be replaced by $S_E = S_3/T$ because of the periodicity of S_E in the Euclidean time, where S_3 is the corresponding three-dimensional Euclidean action [59]. The bubbles can percolate when the probability of the bubble nucleation per unit volume and time is of order one. Since the prefactor A in (25) is $A(T) \propto T^4$ [59], we can translate this condition as

$$\left.\frac{\Gamma}{H^4}\right|_{t=t_{\rm t}} \simeq 1 \;\rightleftarrows\; \frac{S_3(T_{\rm t})}{T_{\rm t}} = 4\ln\left(\frac{T_{\rm t}}{H_{\rm t}}\right), \tag{26}$$

where $H_{\rm t}$ is the Hubble parameter at the transition temperature $T_{\rm t}$.

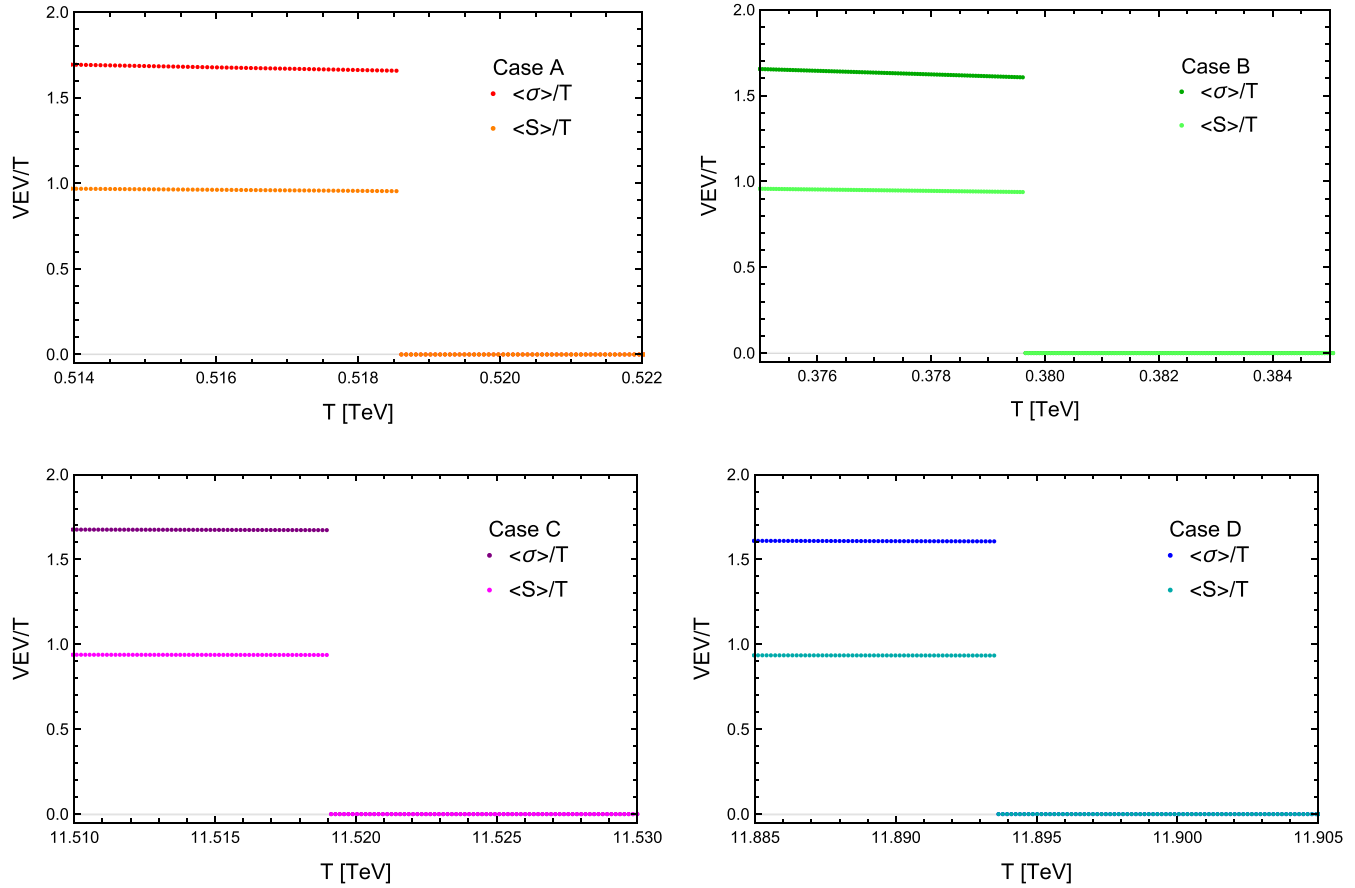

FIG. 3. The temperature dependence of $\langle\sigma\rangle/T$ (dark colored) and $\langle S\rangle/T$ (light colored) for each benchmark point. Cases A (top left), B (top right), C (bottom left), and D (bottom right) are defined in Table I.

The bubble dynamics can be characterized by two parameters, namely, α and β at T_t [18]: α expresses how much energy the phase transition releases, while β^{-1} expresses how long its phase transition takes. These parameters are essential for computing the GW signal from the cosmological phase transition [18]. The parameter α is defined as

$$\alpha \equiv \left.\frac{\epsilon}{\rho_{\rm rad}}\right|_{T=T_t}, \tag{27}$$

which is the ratio of the latent heat ϵ liberated at the phase transition to the thermal energy density $\rho_{\rm rad}(T_t) = (\pi^2/30)g_*(T_t)T_t^4$ in the symmetric phase. The latent heat can be computed from the effective potential at finite temperature as

$$\epsilon(T) \equiv -\Delta V_{\rm EFF}(T) + T\frac{\partial \Delta V_{\rm EFF}(T)}{\partial T}, \tag{28}$$

where $\Delta V_{\rm EFF}(T)$ is the difference of the effective potential between the true and false vacuum. The parameter β is defined as

$$\beta \equiv -\left.\frac{dS_E}{dt}\right|_{t=t_t} \simeq \left.\frac{1}{\Gamma}\frac{d\Gamma}{dt}\right|_{t=t_t}. \tag{29}$$

Using H_t, we can redefine a dimensionless parameter $\tilde{\beta}$ as

$$\tilde{\beta} \equiv \frac{\beta}{H_t} = T_t\frac{d}{dT}\left(\frac{S_3(T)}{T}\right)\bigg|_{T=T_t}. \tag{30}$$

In the following subsections we apply above the general formula (26)–(30) to compute the parameters $(T_t, \alpha, \tilde{\beta})$ for our concrete problem, and we estimate the corresponding GW signal.

A. Bubble nucleation and tunneling parameters

In order to discuss the bubble nucleation which stems from the first-order chiral phase transition, we need to calculate S_3. For this purpose we use the effective Lagrangian for the mean field σ. However, the mean field σ cannot describe tunneling at a tree level, because its kinetic term is absent at the tree level. Hence we compute its kinetic term from the two-point function $\Gamma_{\sigma\sigma}$ at the one-loop level, which is given in (12). First we discuss the zero-temperature case and define the field renormalization constant Z_σ for the σ field as

$$\Gamma_{\sigma\sigma}(p^2) = \Gamma_{\sigma\sigma}(0) + Z_\sigma^{-1}(S,\sigma)p^2 + \mathcal{O}(p^4),$$

where

$$Z_\sigma^{-1}(S,\sigma) = -\left(1-\frac{G_D}{4G^2}\sigma\right)^2 3n_c\frac{d}{dp^2}I_{\varphi^2}(p^2,M;\Lambda_{\rm H})\bigg|_{p^2=0}.$$

Thus the effective Lagrangian for the σ field at zero temperature is

$$\mathcal{L}_\sigma = \frac{Z_\sigma^{-1}(S,\sigma)}{2}\partial_\mu\sigma\partial^\mu\sigma - V_{\rm eff}(S,\sigma), \tag{31}$$

where $V_{\rm eff}(S,\sigma) = V^{h\to 0}_{\rm SM+S}(S) + V_{\rm NJL}(S,\sigma)$ [$V_{\rm NJL}(S,\sigma)$ is given in (9)]. Note that the field renormalization constant Z_σ^{-1} at the symmetric phase ($S=\sigma=0$) diverges (see the Appendix). This is expected, because the composite state σ disappears in the symmetric phase.

As mentioned in the previous section, hidden QCD tunneling should occur in the two-dimensional field space and could be described by the three-dimensional Euclidean action

$$S_3(T) = \int d^3x\left[\frac{Z_\sigma^{-1}(S,\sigma,T)}{2}(\partial_i\sigma)^2 + \frac{1}{2}(\partial_i S)^2 + V_{\rm EFF}(S,\sigma,T)\right]. \tag{32}$$

The field renormalization constant at finite temperature is computed in the Appendix and found to be

$$Z_\sigma^{-1}(S,\sigma,T) = \frac{3n_c}{8\pi^2}\left(1-\frac{G_D}{4G^2}\sigma\right)^2\left[\ln\left(1+\frac{\Lambda_{\rm H}^2}{M^2}\right) + \frac{\Lambda_{\rm H}^2M^2}{(\Lambda_{\rm H}^2+M^2)^2} - 32\pi^2(A_F(u^2)-B_F(u^2))\right], \tag{33}$$

where $u = M/T$, and M, $A_F(u^2)$, and $B_F(u^2)$ are given in Eqs. (7), (A5), and (A6), respectively. In Fig. 4 we show the field dependency of the field renormalization constant $Z_\sigma(S,\sigma,T)$ for $S=0$ and $T/\Lambda_{\rm H} = 0$, 0.01, 0.02, and 0.03, which corresponds to the black, red, blue, and purple line, respectively. As shown in Fig. 4, the field renormalization constant $Z_\sigma(S,\sigma,T)$ vanishes in the symmetric phase. The O(3) symmetric bounce solution can be obtained by solving the equations of motion

$$\frac{d^2\sigma}{dr^2} + \frac{2}{r}\frac{d\sigma}{dr} + \frac{1}{2}\frac{\partial \ln Z_\sigma(S,\sigma,T)}{\partial\sigma}\left(\frac{d\sigma}{dr}\right)^2 = Z_\sigma(S,\sigma,T)\frac{\partial V_{\rm EFF}(S,\sigma,T)}{\partial\sigma}, \tag{34}$$

$$\frac{d^2S}{dr^2} + \frac{2}{r}\frac{dS}{dr} - \frac{1}{2}\frac{\partial Z_\sigma^{-1}(S,\sigma,T)}{\partial S}\left(\frac{d\sigma}{dr}\right)^2 = \frac{\partial V_{\rm EFF}(S,\sigma,T)}{\partial S}, \tag{35}$$

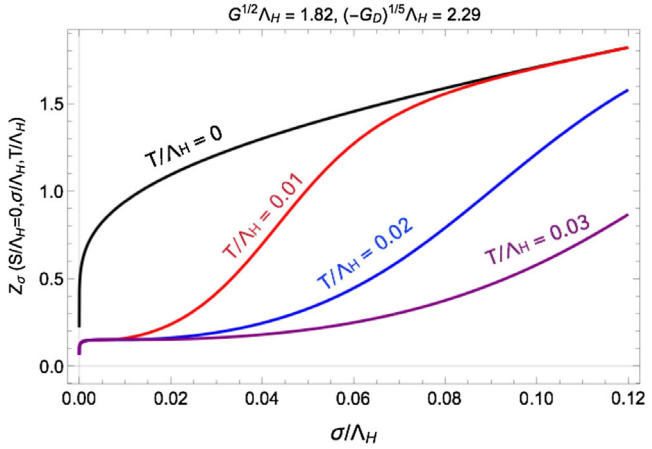

FIG. 4. The σ field dependence of the field renormalization constant $Z_\sigma(S=0,\sigma,T)$ for $T/\Lambda_{\rm H}=0$, (black), 0.01 (red), 0.02 (blue), and 0.03 (purple).

where $r=(x_1^2+x_2^2+x_3^2)^{1/2}$. The boundary conditions are

$$\left.\frac{d\sigma}{dr}\right|_{r=0}=0,\quad \left.\frac{dS}{dr}\right|_{r=0}=0,\quad \lim_{r\to\infty}\sigma(r)=0,\quad \lim_{r\to\infty}S(r)=0, \tag{36}$$

where the coordinate of the symmetric minimum (false vacuum) of the potential is chosen at the origin of the σ-S space. Note that the field renormalization constant $Z_\sigma(S,\sigma,T)$ does not depend explicitly on r but also depends on the fields.

B. Computation of multidimensional bounce solution

In the one-dimensional case we can obtain a bounce solution by using the so-called overshooting/undershooting method [17]. However, this is a cumbersome method in the multidimensional case, because two initial conditions have to be simultaneously fine-tuned. Instead, we here employ an approach similar to the path deformation method [60].

The bounce solution is unique. That is, $\sigma(r)$ and $S(r)$, which satisfy the differential Eqs. (34) and (35) with the boundary conditions (36), are a unique function of r. If we assume that $\sigma(r)$ is an invertible function for $r\in[0,\infty)$, then there exists a unique inverse of σ, which we denote by σ^{-1}. That is, $\sigma^{-1}\circ\sigma$ is the identity function, or $r=\sigma^{-1}(\sigma(r))$. Because of this assumption, S can be regarded as a function of σ, i.e., $S(\sigma)$.[5] Therefore, (34) and (35) can be written as, respectively,

$$\frac{d^2\sigma}{dr^2}+\frac{2}{r}\frac{d\sigma}{dr}+\frac{1}{2}\frac{\partial\ln Z_\sigma(S(\sigma),\sigma,T)}{\partial\sigma}\left(\frac{d\sigma}{dr}\right)^2=F_\sigma(S(\sigma),\sigma), \tag{37}$$

[5]We use the same symbol S for the functions of r and σ.

$$\frac{d^2S}{d\sigma^2}\left(\frac{d\sigma}{dr}\right)^2+\left(\frac{dS}{d\sigma}\right)\left(\frac{d^2\sigma}{dr^2}+\frac{2}{r}\frac{d\sigma}{dr}\right)-\frac{1}{2}\frac{\partial Z_\sigma^{-1}(S(\sigma),\sigma,T)}{\partial S}\left(\frac{d\sigma}{dr}\right)^2=F_S(S(\sigma),\sigma), \tag{38}$$

where $F_\sigma(S(\sigma),\sigma)$ and $F_S(S(\sigma),\sigma)$ are the rhs of (34) and (35), respectively, and we have suppressed the T dependence of $F_\sigma(S(\sigma),\sigma)$ and $F_S(S(\sigma),\sigma)$. The point is that if $S(\sigma)$ is given, then (37) is a one-dimensional differential equation and hence can be solved by applying the overshooting/undershooting method. If $S(\sigma)$ is the true solution of the problem, it should satisfy (38) with $\sigma(r)$ obtained from (37) as well, which means that

$$N(r)=0 \tag{39}$$

is also satisfied, where

$$N(r)=\frac{d^2S}{d\sigma^2}(r)\left(\frac{d\sigma}{dr}(r)\right)^2+\frac{dS}{d\sigma}(r)F_\sigma(S,\sigma)(r)-F_S(S,\sigma)(r)-\frac{1}{2}\left(\frac{d\sigma}{dr}(r)\right)^2\left(\frac{\partial Z_\sigma^{-1}(S,\sigma,T)}{\partial S}(r)+\frac{dS}{d\sigma}(r)\frac{\partial\ln Z_\sigma(S,\sigma,T)}{\partial\sigma}(r)\right). \tag{40}$$

Since the one-dimensional differential Eq. (37) for a given path $S(\sigma)$ can be simply solved, our task is to find $S(\sigma)$ which satisfies (39). We do this in an iterative way. We start with a linear function $S_0(\sigma)$, which connects the true and false vacuum:

$$S_0(\sigma)=\frac{S^B-S^S}{\sigma^B-\sigma^S}(\sigma-\sigma^S)+S^S, \tag{41}$$

where $(S^{B,S},\sigma^{B,S})$ (with $S^S=\sigma^S=0$) are the positions of the true and false vacuum, respectively. Then we solve (37) with the path $S(\sigma)=S_0(\sigma)$ and denote the bounce solution by $\sigma_0(r)$. Note that $\sigma_0(0)$ is no longer σ^B, so that the end point of $S_0(\sigma)$ on the true vacuum side is no longer S^B, i.e., $S_0(\sigma_0(0))\neq S^B$. Next we compute the rhs of (40) using $\sigma_0(r)$ and $S_0(\sigma_0(r))$ for σ and $S(\sigma)$, respectively, and we denote it by $N_0(r)$. Since $S_0(\sigma_0(r))$ is not the true solution of the problem, $N_0(r)$ does not vanish. Knowing $N_0(r)$, we have to define the next step of the iteration:

$$S_1(\sigma)=S_0(\sigma)+\Delta S_0(\sigma). \tag{42}$$

To proceed we assume that not only the true solution $\sigma(r)$ but also $\sigma_0(r)$ is an invertible function, so that $N_0(r)$ can be written as a function of σ, i.e.,

$$\hat{N}_0(\sigma)\equiv N_0(r=\sigma_0^{-1}(\sigma)). \tag{43}$$

Note that because of the σ and S dependence of $Z_\sigma(S,\sigma,T)$ (partly shown in Fig. 4) and also of $V_{\rm EFF}(S,\sigma,T)$, $\hat{N}_0(\sigma)$ vanishes at the false vacuum, i.e., at $\sigma=0$ (S also vanishes at $\sigma=0$). Further, if $\hat{N}_0(\sigma)$ vanishes at some nonzero values of σ, the deformation $\Delta S_0(\sigma)$ should also vanish at these values of σ. This brings us to assume that $\Delta S_0(\sigma)$ is proportional to $\hat{N}_0(\sigma)$. Therefore, the path $S_{i+1}(\sigma)$ in the $(i+1)$th step can be defined as

$$S_{i+1}(\sigma)=S_i(\sigma)+k\hat{N}_i(\sigma), \tag{44}$$

where k is the step size, and $\hat{N}_i(\sigma)=N_i(r=\sigma_i^{-1}(\sigma))$. Note that $S_{i+1}(\sigma)$ satisfies the boundary condition $\lim_{\sigma\to 0}S_{i+1}(\sigma)=0$. To obtain $\sigma_{i+1}(r)$, the initial value of $\sigma_{i+1}(0)$ has to be fine-tuned in such away that $d\sigma_{i+1}(r)/dr|_{r=0}=0$ and $\lim_{r\to\infty}\sigma_{i+1}(r)=0$ are satisfied. If $d\sigma_{i+1}(r)/dr|_{r=0}=0$ is satisfied, $dS_{i+1}(\sigma_{i+1}(r))/dr|_{r=0}=0$ is automatically satisfied. Since $\sigma_{i+1}(0)$ is different from $\sigma_i(0)$, the end point of $S_{i+1}(\sigma)$ on the true vacuum side is also moved to $S_{i+1}(\sigma_{i+1}(0))$.

Since the assumptions we made above cannot be rigorously justified, there is no guarantee that the steps converge to the true solution of the problem. In fact, if we choose the wrong sign for k, steps diverge or do not converge. We have checked our method for a number of examples and found that once we use an appropriate sign and size for k, the steps can converge, where we approximate the path $S_i(\sigma)$ (which is obtained numerically) with a fifth-degree polynomial in σ as in [28]. In Fig. 5, we present the numerical solution $S_{15}(\sigma)$ (black solid line) with $|k\hat{N}_{15}(\sigma)|/S_{15}(\sigma)<10^{-2}$ obtained from $S_0(\sigma)$ (black dashed line) in the two-dimensional field space at $T=0.390$ TeV [below the critical temperature $T=0.519$ TeV as shown in Fig. 3 (top left)] for Case A.[6] The corresponding bounce solution as a function of r is shown in Fig. 6. The Euclidean action (32) obtained from the bounce solution is $S_3(T)/T=148.2$, where the difference of $S_3(T)/T$ between the 14th and 15th steps is less than a few percent. Computing $S_3(T)/T$ for each temperature as in the above method, we can find the transition temperature $T_{\rm t}$ from the condition (26), which is used for the determination of tunneling parameters α and $\tilde{\beta}$ given in Eqs. (27) and (30).

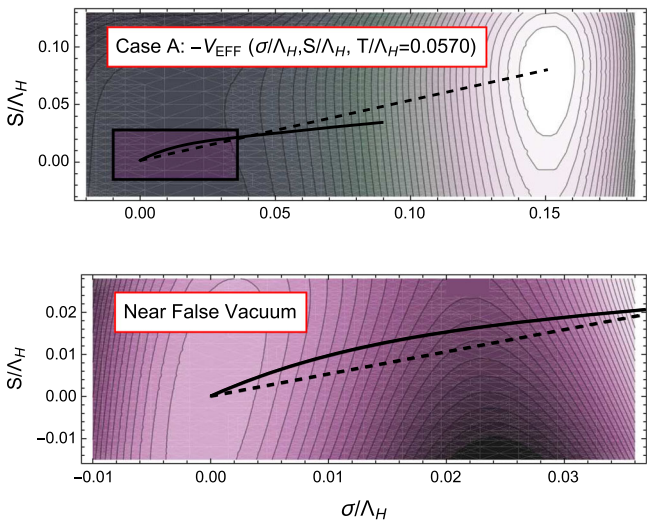

FIG. 5. Top: The contour plot of the effective potential $V_{\rm EFF}$ in (17) with $T/\Lambda_{\rm H}=0.0570$ for Case A, defined in Table I. The black dashed line stands for the initial path $S_0(\sigma)$ and the black solid line is the path $S_{15}(\sigma)$ with $|k\hat{N}_{15}(\sigma)|/S_{15}(\sigma)<10^{-2}$. Bottom: The region enclosed by the box near the false vacuum in the top figure is zoomed.

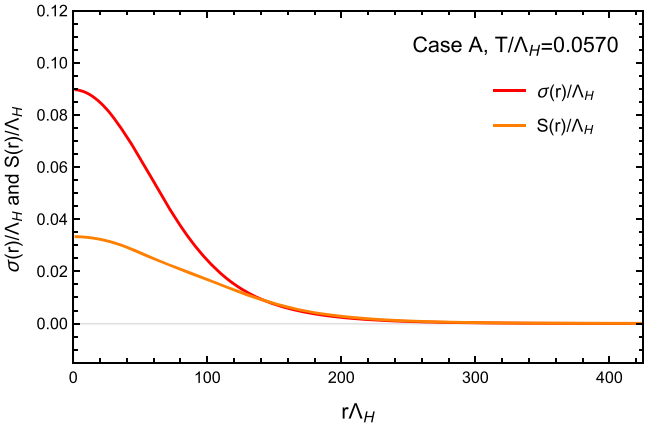

FIG. 6. The bounce solution for Case A with $T/\Lambda_{\rm H}=0.0570$. The red line stands for $\sigma(r)/\Lambda_{\rm H}$, and the orange one for $S(r)/\Lambda_{\rm H}$, which correspond to the path $S_{15}(\sigma)$ (black solid line) shown in Fig. 5.

C. Tunneling parameters for the benchmark points

The GW spectrum produced by a first-order phase transition can be characterized by the released energy and its duration time, and it is known that they can be parametrized by the set of the parameters $(T_{\rm t},\alpha,\tilde{\beta})$. The results for the benchmark points are given in Table II. We see from Table II that α and $\tilde{\beta}^{-1}$ for Cases A and C are larger than those for Cases B and D. Recalling the parameter values for the benchmark points (Table I), we can infer that the smaller the explicit chiral symmetry breaking (the smaller y) is, the larger α and $\tilde{\beta}^{-1}$ are. This suggests that the parameters of the model can be constrained if the GW is measured with a certain accuracy.

IV. SIGNAL FROM THE HIDDEN SECTOR QCD

Finally we come to our main purpose: to check the testability of the GW background produced by the first-order phase transitions in the hidden sector. There coexist three processes contributing to the stochastic GW background spectrum:

[6] $|k\hat{N}_i(\sigma)|/S_i(\sigma)<10^{-2}$ is not satisfied for $i<15$.

$$h^2\Omega_{\rm GW} = h^2\Omega_\varphi + h^2\Omega_{\rm sw} + h^2\Omega_{\rm turb}, \tag{45}$$

where h is the dimensionless Hubble parameter, Ω_φ stands for the scalar field contribution from collisions of bubble walls [61–66], $\Omega_{\rm sw}$ for the contribution from sound waves in plasma after the bubble collisions [67–70], and $\Omega_{\rm turb}$ for the contribution from magnetohydrodynamic (MHD) turbulence in plasma [71–74]. Following [12], each contribution is given for a given set of the parameters $(T_{\rm t}, \alpha, \tilde{\beta})$ with the velocity of bubble wall v_w and the κ_φ, κ_v, and $\kappa_{\rm turb}$ which are the fraction of vacuum energy, respectively, converted into gradient energy of scalar field, bulk motion of the fluid, and MHD turbulence.

(i) Scalar field contribution Ω_φ:

$$h^2\Omega_\varphi(f) = 1.67\times10^{-5}\tilde{\beta}^{-2}\left(\frac{\kappa_\varphi\alpha}{1+\alpha}\right)^2\left(\frac{100}{g_*}\right)^{1/3} \times\left(\frac{0.11v_w^3}{0.42+v_w^2}\right)S_\varphi(f), \tag{46}$$

where the spectral shape of the peak frequency f_φ is

$$S_\varphi(f) = \frac{3.8(f/f_\varphi)^{2.8}}{1+2.8(f/f_\varphi)^{3.8}} \tag{47}$$

with the peak frequency

$$f_\varphi = 16.5\times10^{-6}\tilde{\beta}\left(\frac{0.62}{1.8-0.1v_w+v_w^2}\right) \times\left(\frac{T_{\rm t}}{100\ {\rm GeV}}\right)\left(\frac{g_*}{100}\right)^{1/6}{\rm Hz}. \tag{48}$$

(ii) Sound wave contribution $\Omega_{\rm sw}$:

$$h^2\Omega_{\rm sw}(f) = 2.65\times10^{-6}\tilde{\beta}^{-1}\left(\frac{\kappa_v\alpha}{1+\alpha}\right)^2\left(\frac{100}{g_*}\right)^{1/3} \times v_w S_{\rm sw}(f), \tag{49}$$

where the spectral shape of the peak frequency $f_{\rm sw}$ is

$$S_{\rm sw}(f) = (f/f_{\rm sw})^3\left(\frac{7}{4+3(f/f_{\rm sw})^2}\right)^{7/2} \tag{50}$$

with the peak frequency

$$f_{\rm sw} = 1.9\times10^{-5}v_w^{-1}\tilde{\beta}\left(\frac{T_{\rm t}}{100\ {\rm GeV}}\right)\left(\frac{g_*}{100}\right)^{1/6}{\rm Hz}. \tag{51}$$

(iii) MHD turbulence contribution $\Omega_{\rm turb}$:

$$h^2\Omega_{\rm turb}(f) = 3.35\times10^{-4}\tilde{\beta}^{-1}\left(\frac{\kappa_{\rm turb}\alpha}{1+\alpha}\right)^{\frac{3}{2}}\left(\frac{100}{g_*}\right)^{1/3} \times v_w S_{\rm turb}(f), \tag{52}$$

where the spectral shape of the peak frequency $f_{\rm turb}$ is

$$S_{\rm turb}(f) = \frac{(f/f_{\rm turb})^3}{[1+(f/f_{\rm turb})]^{\frac{11}{3}}(1+8\pi f/h_{\rm t})} \tag{53}$$

with the peak frequency

$$f_{\rm turb} = 2.7\times10^{-5}v_w^{-1}\tilde{\beta}\left(\frac{T_{\rm t}}{100\ {\rm GeV}}\right)\left(\frac{g_*}{100}\right)^{1/6}{\rm Hz}, \tag{54}$$

and

$$h_{\rm t} = 16.5\times10^{-6}\left(\frac{T_{\rm t}}{100\ {\rm GeV}}\right)\left(\frac{g_*}{100}\right)^{1/6}{\rm Hz}, \tag{55}$$

which is the value (redshifted to today) of the inverse Hubble time at the GW production.

Bubbles produced by quantum tunneling grow with velocity v_w. It is even possible for v_w to approach continuously to the speed of light (runaway configuration) [75,76]. In a no-runaway case, the bubble wall velocity v_w terminates at a certain velocity < 1. The criterion for runaway bubbles is the value of α compared with α_∞ (the minimum value of α for runaway bubbles):

(i) $\alpha_\infty > \alpha$: No runaway bubbles ($h^2\Omega_{\rm GW} \simeq h^2\Omega_{\rm sw} + h^2\Omega_{\rm turb}$)

(ii) $\alpha_\infty < \alpha$: Runaway bubbles ($h^2\Omega_{\rm GW} \simeq h^2\Omega_\varphi + h^2\Omega_{\rm sw} + h^2\Omega_{\rm turb}$),

where α_∞ is given by [12,77]

$$\alpha_\infty \simeq \frac{30}{24\pi^2}\frac{\sum_a c_a\Delta m_a^2(\varphi)}{g_*T_{\rm t}^2}. \tag{56}$$

TABLE II. The parameters $(T_{\rm t}, \alpha, \tilde{\beta})$ for benchmark points defined in Table I. The transition temperature $T_{\rm t}$, the ratio of the latent heat to the thermal energy density α, and the dimensionless inverse duration time $\tilde{\beta}$ are defined by Eqs. (26), (27), and (30), respectively.

Case	$T_{\rm t}$ (TeV)	α	$\tilde{\beta}$
A	0.387	0.288	8.24×10^2
B	0.306	0.223	14.86×10^2
C	8.731	0.310	7.15×10^2
D	9.480	0.232	13.29×10^2

Here c_a is the degree of freedom of the particle a (which should be multiplied with $1/2$ in the fermionic case in addition), and $\Delta m_a^2(\varphi)$ is the difference of its field-dependent squared masses in two phases. For our model with $g_* = 115.75$ we use

$$\alpha_\infty \simeq 1.09 \times 10^{-3} \left[n_f \left(\frac{2M(\langle \varphi_i \rangle)}{T_t} \right)^2 + 3\lambda_S \left(\frac{\langle S \rangle}{T_t} \right)^2 \right]. \quad (57)$$

Here we have used the relation $m_\sigma^2 \simeq (2M)^2$, where the constituent mass M is given in Eq. (7). This relation is approximately satisfied, because we have neglected the contribution from the Yukawa coupling y (which is very small for our benchmark parameters). We have computed α_∞ for the benchmark points and found

$$\alpha_\infty = \begin{cases} \text{Case A: } 0.116 & \text{Case C : } 0.125 \\ \text{Case B : } 0.092 & \text{Case D: } 0.095 \end{cases}. \quad (58)$$

Comparing α given in Table II with α_∞ for each benchmark point we see that the bubbles for all cases run away. With α_∞ given above we can then compute the fraction κ of the latent heat converted to the relevant contribution to the GW spectrum [12]:

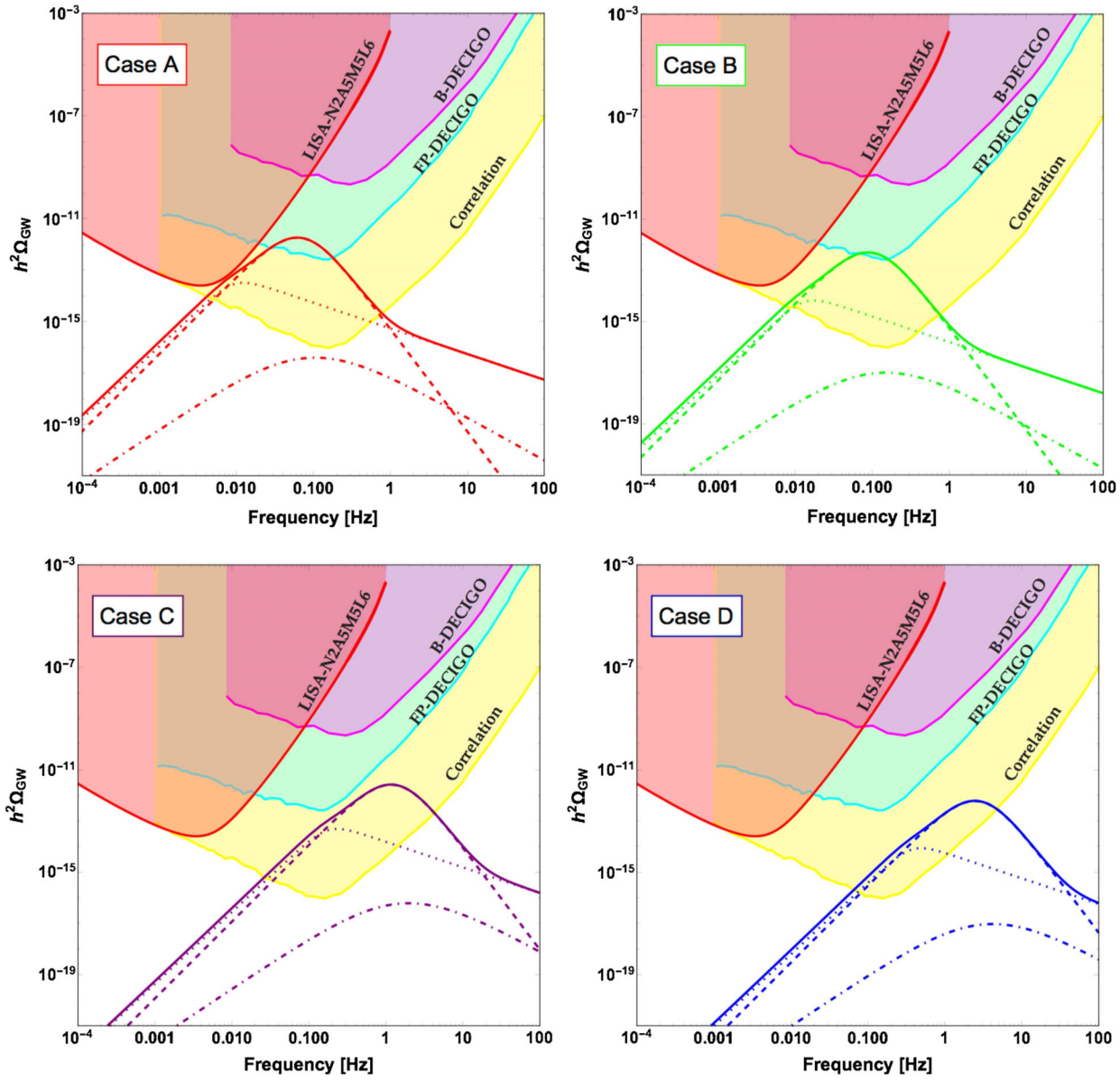

FIG. 7. The GW spectrum with $v_w = 1$ for Case A (top left), B (top right), C (bottom left), and D (bottom right). The total GW spectrum (solid lines) is the sum of the sound wave (dashed lines), scalar (dotted lines), and MHD turbulence (dashed-dotted lines) contributions. The colored regions are observable regions of LISA (LISA-N2A5M5L6 [12]) and DECIGO (B-DECIGO, FP-DECIGO, and Correlation [14–16]).

$$\kappa_\varphi \equiv 1 - \frac{\alpha_\infty}{\alpha}, \qquad \kappa_v \equiv \frac{\alpha_\infty}{\alpha}\kappa_\infty, \qquad \kappa_{\rm turb} = \epsilon\kappa_v,$$
$$\kappa_\infty \equiv \frac{\alpha_\infty}{0.73 + 0.083\sqrt{\alpha_\infty} + \alpha_\infty}, \tag{59}$$

where for all the benchmark cases (being all runaway) we have assumed that the wall velocity v_w is close to the speed of light, and $\epsilon = 0.05$ [12] for the MHD turbulence. With Eqs. (46)–(55), (58), and (59) we are now in position to compute the GW signal for the benchmark cases.

In Fig. 7 we present our results. For each benchmark case (A–D) we show the GW spectrum with $v_w = 1$, where the total GW signal, sound wave, scalar, and MHD turbulence contributions are denoted by the solid, dashed, dotted, and dashed-dotted lines, respectively. The colored regions show observable regions of different configurations of LISA [12,13] and DECIGO [14–16]. The label of "LISA-N2A5M5L6" corresponds to the configuration of LISA provided in Table 1 in [12], while the labels "B-DECIGO," "FP-DECIGO," and "Correlation" are DECIGO designs [14–16]. As we can see from Fig. 7, the sound wave contribution is dominant for all the cases, while the MHD turbulence contribution is negligibly small, so that the peak frequency of the GW spectrum is basically that of the sound wave contribution. The contribution MHD turbulence is small because ϵ (the fraction of turbulent bulk motion) is set to 0.05 [12]. The scalar contribution becomes non-negligible at higher frequencies and consequently changes the slope for this region of frequency. But since it depends on $\tilde{\beta}^{-2}$ [see Eq. (46)], the sound wave contribution being proportional to $\tilde{\beta}^{-1}$ is larger for smaller $\tilde{\beta}$. The peak frequencies of Cases A and B are ∼0.1 Hz, while those of C and D are a few hertz. The main reason for this difference is the different transition temperature $T_{\rm t}$ (see Table II), which once again results from the difference of

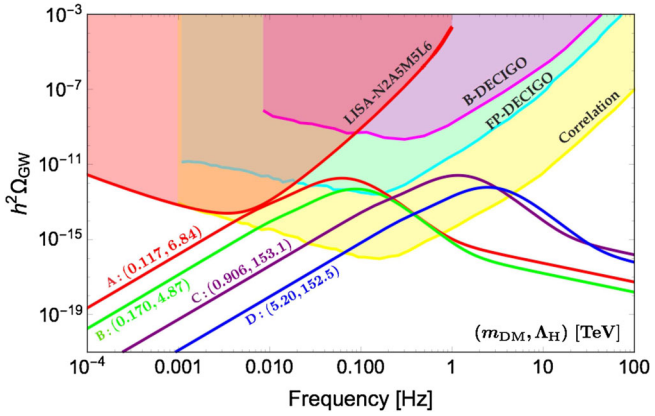

FIG. 8. The GW spectrum with $v_w = 1$ for Case A (red), B (green), C (purple), and D (blue). The numbers in the parentheses are $m_{\rm DM}$ and $\Lambda_{\rm H}$ in units of TeV (Table I). The colored regions are observable regions of LISA (LISA-N2A5M5L6 [12]) and DECIGO (B-DECIGO, FP-DECIGO, and Correlation [14–16]).

λ_{HS} (see Table I). Consequently, the GW signal is difficult to observe at LISA [12,13]. The peak values of the GW spectrum are 10^{-12} for A and C, while those for B and D are 10^{-13}. Therefore, DECIGO sensitivities [14–16] may be sufficient to observe the signal. Finally we summarize the results for Cases A–D in Fig. 8 with the DM mass $m_{\rm DM}$ and the hidden QCD scale $\Lambda_{\rm H}$. If Cases A and B, and also C and D, could be experimentally distinguished, we could obtain information about the magnitude of the explicit chiral symmetry breaking in the hidden sector.

V. SUMMARY AND CONCLUSION

Mass can be created by nonperturbative effects in non-Abelian gauge theories from nothing. By "from nothing" we mean that the theory has no dimensional parameter and hence is scale invariant at the classical level. Scale invariance is broken explicitly by a scale anomaly and at the same time dynamically by the nonperturbative effects. Dynamical breaking of scale invariance can be used to explain the origin of the Higgs mass as well as of the DM mass [42–48,78–81].

Needless to say, dynamical breaking of scale invariance is associated with a phase transition at finite temperature [42,54,79]. If the phase transition is of first order and strong enough in the early Universe, it can produce GW which might be observed today as a GW background [8].

In this paper we have expanded our analysis of a particular scale invariant extension of the SM to include the aspect of the GW background predicted by the model. The model contains a strongly interacting hidden sector, described by a non-Abelian gauge theory, in which a mass scale in the TeV region is generated through the chiral symmetry breaking in the hidden sector. The corresponding (pseudo) NG bosons are a realistic candidate for DM, since their mass is finite because the chiral symmetry is also explicitly broken by a Yukawa coupling between the hidden sector fermions and a SM singlet real scalar field S. The scalar field S plays the role of a mediator that transfers the robust energy scale from the hidden sector to the SM sector via a Higgs portal coupling.

As in [42,43] we have used the NJL method to effectively treat the DχSB. Integrating out the hidden sector fermions in the NJL model yields an effective potential for the chiral condensate at zero and finite temperature. In the mean field approximation we can identify the chiral condensate with σ and the NG bosons with ϕ_a (which are DM). We have restricted ourselves to $n_c = n_f = 3$ for the hidden sector QCD, because we can simply scale up the parameters of the NJL model for the real QCD, such that the hidden sector NJL model has the same number of independent parameters as that of the hidden sector QCD.

As it is known, the nature of the chiral phase transition changes depending on the strength of the explicit chiral symmetry braking. For the hidden sector QCD it means, on one hand, that the Yukawa coupling constant y should be

sufficiently small to obtain a strong first-order chiral phase transition. On the other hand, a small y implies two-stage phase transitions: the chiral phase transition at $T \gtrsim \mathcal{O}(1)$ TeV and the EW phase transition at $T \sim \mathcal{O}(100)$ GeV. That is, two phase transitions can be clearly distinguished.

Using the technique in the literature (see [12] and references therein) within the framework of the NJL model in the mean field approximation, we have analyzed the GW background produced by the chiral phase transition in the hidden sector of the model. In particular, depending on the value of y and of the Higgs portal coupling λ_{HS}, we have chosen four benchmark points in the parameter space. These points are representative points characterized by the magnitude of the explicit chiral symmetry breaking and the hidden sector scale $\Lambda_{\rm H}$. We have found for these points that the peaks of the GW signal appear at frequencies $\mathcal{O}(0.01-1)$ Hz. Unfortunately, these frequencies are slightly too high, so that it will be difficult for them to be observed at LISA [12,13]. But their strength seems to be sufficiently large for observations at DECIGO [14–16], which will cover a higher frequency region. We emphasize that observation of a GW background signal at frequencies $0.1 \sim$ few hertz with $h^2\Omega_{\rm GW} \gtrsim 10^{-13}$ may be a strong indication for strongly interacting hidden sector models.

Finally we should admit that our results have been obtained by using the NJL model, which is supposed to serve as an effective theory of the hidden sector QCD. A fair question is about the systematic uncertainties present in this approach. At the moment we can say only that the NJL model for the real hadrons can reproduce their basic quantities with an uncertainty of $\mathcal{O}(10-20)\%$ [53]. Therefore, to make more precise predictions it is certainly inevitable to use a more reliable method such as lattice gauge theory.

ACKNOWLEDGMENTS

We thank Thomas Konstandin for useful discussions. The work of M. A. is supported in part by the Japan Society for the Promotion of Sciences Grant-in-Aid for Scientific Research (Grants No. 16H00864 and No. 17K05412). J. K. is partially supported by the Grant-in-Aid for Scientific Research (C) from the Japan Society for Promotion of Science (Grant No. 16K05315).

Note added.—The recent paper [82] is certainly relevant to us, but the paper appeared after we completed our calculations.

APPENDIX: THERMAL FUNCTION FOR FIELD RENORMALIZATION CONSTANT

The field renormalization can be computed as

$$Z_\sigma^{-1}(S,\sigma) = -\left(1-\frac{G_D}{4G^2}\sigma\right)^2 3n_c \frac{d}{dp^2} I_{\varphi^2}(p^2,M;\Lambda_{\rm H})\Big|_{p^2=0},$$

where the loop function $I_{\varphi^2}(p^2,M)$ is given in Eq. (13) and its derivative can be written as

$$\begin{aligned}\frac{d}{dp^2} I_{\varphi^2}(p^2,M)\Big|_{p^2=0} &= -4\int \frac{d^4k}{i(2\pi)^4}\frac{1}{(k^2-M^2)^2} + 4\int \frac{d^4k}{i(2\pi)^4}\frac{2M^2}{(k^2-M^2)^3} \\ &\equiv -4I_A(M) + 4I_B(M),\end{aligned}$$

where we defined two terms as I_A and I_B. Using the standard calculation method at finite temperature, they can be computed as

$$\begin{aligned}I_A &= \frac{T}{2\pi i}\oint_C \frac{d^3k}{(2\pi)^3}\frac{1}{(k_0^2-\omega^2)^2}\frac{1}{2}\beta\tanh\left(\frac{1}{2}\beta k_0\right) \\ &= A_F^0(M;\Lambda_{\rm H}) + A_F(u^2),\end{aligned} \tag{A1}$$

$$\begin{aligned}I_B &= \frac{T}{2\pi i}\oint_C \frac{d^3k}{(2\pi)^3}\frac{2M^2}{(k_0^2-\omega^2)^3}\frac{1}{2}\beta\tanh\left(\frac{1}{2}\beta k_0\right) \\ &= B_F^0(M;\Lambda_{\rm H}) + B_F(u^2),\end{aligned} \tag{A2}$$

where $\beta = 1/T$, $k_0 = i\omega_n = i\pi(2n+1)T$, $u = M/T$, and the function $\frac{1}{2}\beta\tanh(\frac{1}{2}\beta k_0)$ has a pole at k_0. The zero-temperature components with four-dimensional cutoff are

$$\begin{aligned}A_F^0(M;\Lambda_{\rm H}) &= \int_{\Lambda_{\rm H}} \frac{d^4k_E}{(2\pi)^4}\frac{1}{(k_E^2+M^2)^2} \\ &= \frac{1}{(4\pi)^2}\frac{1}{2}\left[\ln\left(1+\frac{\Lambda_{\rm H}^2}{M^2}\right) - \frac{\Lambda_{\rm H}^2}{\Lambda_{\rm H}^2+M^2}\right],\end{aligned} \tag{A3}$$

$$\begin{aligned}B_F^0(M;\Lambda_{\rm H}) &= -\int_{\Lambda_{\rm H}} \frac{d^4k_E}{(2\pi)^4}\frac{2M^2}{(k_E^2+M^2)^3} \\ &= -\frac{1}{(4\pi)^2}\frac{\Lambda_{\rm H}^4}{2(\Lambda_{\rm H}^2+M^2)^2},\end{aligned} \tag{A4}$$

and those thermal effect functions can be written as

$$\begin{aligned}A_F(u^2) &= \int_{-i\infty+\epsilon}^{i\infty+\epsilon}\frac{dk_0}{2\pi i}\int\frac{d^3k}{(2\pi)^3}\frac{2}{(k_0-\omega)^2(k_0+\omega)^2}\frac{1}{e^{\beta k_0}+1} \\ &= -\frac{1}{4\pi^2}\int_0^\infty dx\frac{x^2}{(\sqrt{x^2+u^2})^3}\frac{1}{1+e^{\sqrt{x^2+u^2}}} \\ &\quad\times\frac{1}{8\pi^2}\int_0^\infty dx\frac{x^2}{(\sqrt{x^2+u^2})^2}\frac{1}{1+\cosh\sqrt{x^2+u^2}},\end{aligned} \tag{A5}$$

$$B_F(u^2) = \int_{-i\infty+\epsilon}^{i\infty+\epsilon} \frac{dk_0}{2\pi i} \int \frac{d^3k}{(2\pi)^3} \frac{4M^2}{(k_0-\omega)^3(k_0+\omega)^3} \frac{1}{e^{\beta k_0}+1}$$
$$= \frac{2u^2}{\pi^2}\left[3\int_0^\infty dx \frac{x^2}{(\sqrt{x^2+u^2})^5}\frac{1}{1+e^{\sqrt{x^2+u^2}}} + 3\int_0^\infty dx \frac{x^2}{(\sqrt{x^2+u^2})^4}\frac{1}{1+\cosh\sqrt{x^2+u^2}}\right.$$
$$\left. + \int_0^\infty dx \frac{x^2}{(\sqrt{x^2+u^2})^3}\frac{1}{1+\cos\sqrt{x^2+u^2}}\tanh\left(\frac{1}{2}\sqrt{x^2+u^2}\right)\right]. \quad \text{(A6)}$$

In this work we fitted each thermal function using the following fitting functions,

$$A_F(u^2) = \frac{1}{8\pi^2}\ln u + e^{-u}\sum_{n=0}^{40} a_n u^n, \quad \text{(A7)}$$

$$B_F(u^2) = e^{-u}\sum_{n=0}^{40} b_n u^n. \quad \text{(A8)}$$

[1] ATLAS Collaboration, https://twiki.cern.ch/twiki/bin/view/AtlasPublic/Winter201713TeV.

[2] CMS Collaboration, https://cms.cern/news/cms-new-results-Moriond-2017.

[3] D. S. Akerib *et al.* (LUX Collaboration), Results from a Search for Dark Matter in the Complete LUX Exposure, Phys. Rev. Lett. **118**, 021303 (2017).

[4] E. Aprile *et al.* (XENON Collaboration), First Dark Matter Search Results from the XENON1T experiment, arXiv: 1705.06655.

[5] B. P. Abbott *et al.* (LIGO Scientific and Virgo Collaborations), Observation of Gravitational Waves from a Binary Black Hole Merger, Phys. Rev. Lett. **116**, 061102 (2016).

[6] A. A. Starobinsky, Spectrum of relict gravitational radiation and the early state of the Universe, Pis'ma Zh. Eksp. Teor. Fiz. **30**, 719 (1979) JETP Lett. **30**, 682 (1979).

[7] A. Vilenkin and E. P. S. Shellard, *Cosmic Strings and Other Topological Defects* (Cambridge University Press, Cambridge, England, 2000).

[8] E. Witten, Cosmic Separation of Phases, Phys. Rev. D **30**, 272 (1984).

[9] K. Kajantie, M. Laine, K. Rummukainen, and M. E. Shaposhnikov, The electroweak phase transition: A non-perturbative analysis, Nucl. Phys. **B466**, 189 (1996).

[10] K. Kajantie, M. Laine, K. Rummukainen, and M. E. Shaposhnikov, Is There a Hot Electroweak Phase Transition at m(H) Larger or Equal to m(W)?, Phys. Rev. Lett. **77**, 2887 (1996).

[11] K. Rummukainen, M. Tsypin, K. Kajantie, M. Laine, and M. E. Shaposhnikov, The universality class of the electroweak theory, Nucl. Phys. **B532**, 283 (1998).

[12] C. Caprini *et al.*, Science with the space-based interferometer eLISA. II: Gravitational waves from cosmological phase transitions, J. Cosmol. Astropart. Phys. 04 (2016) 001.

[13] H. Audley *et al.*, Laser Interferometer Space Antenna, arXiv:1702.00786.

[14] N. Seto, S. Kawamura, and T. Nakamura, Possibility of Direct Measurement of the Acceleration of the Universe Using 0.1-Hz Band Laser Interferometer Gravitational Wave Antenna in Space, Phys. Rev. Lett. **87**, 221103 (2001).

[15] S. Kawamura *et al.*, The Japanese space gravitational wave antenna DECIGO, Classical Quantum Gravity **23**, S125 (2006).

[16] S. Kawamura *et al.*, The Japanese space gravitational wave antenna: DECIGO, Classical Quantum Gravity **28**, 094011 (2011).

[17] R. Apreda, M. Maggiore, A. Nicolis, and A. Riotto, Gravitational waves from electroweak phase transitions, Nucl. Phys. **B631**, 342 (2002).

[18] C. Grojean and G. Servant, Gravitational Waves from Phase Transitions at the Electroweak Scale and Beyond, Phys. Rev. D **75**, 043507 (2007).

[19] J. R. Espinosa, T. Konstandin, J. M. No, and M. Quiros, Some Cosmological Implications of Hidden Sectors, Phys. Rev. D **78**, 123528 (2008).

[20] A. Ashoorioon and T. Konstandin, Strong electroweak phase transitions without collider traces, J. High Energy Phys. 07 (2009) 086.

[21] S. Das, P. J. Fox, A. Kumar, and N. Weiner, The Dark Side of the Electroweak Phase Transition, J. High Energy Phys. 11 (2010) 108.

[22] P. Schwaller, Gravitational Waves from a Dark Phase Transition, Phys. Rev. Lett. **115**, 181101 (2015).

[23] M. Kakizaki, S. Kanemura, and T. Matsui, Gravitational waves as a probe of extended scalar sectors with the first order electroweak phase transition, Phys. Rev. D **92**, 115007 (2015).

[24] R. Jinno and M. Takimoto, Probing classically conformal $B-L$ model with gravitational waves, Phys. Rev. D **95**, 015020 (2017).

[25] K. Hashino, M. Kakizaki, S. Kanemura, and T. Matsui, Synergy between measurements of gravitational waves and

the triple-Higgs coupling in probing the first-order electroweak phase transition, Phys. Rev. D **94**, 015005 (2016).
[26] J. Kubo and M. Yamada, Scale genesis and gravitational wave in a classically scale invariant extension of the standard model, J. Cosmol. Astropart. Phys. 12 (2016) 001.
[27] V. Vaskonen, Electroweak baryogenesis and gravitational waves from a real scalar singlet, Phys. Rev. D **95**, 123515 (2017).
[28] A. Beniwal, M. Lewicki, J. D. Wells, M. White, and A. G. Williams, Gravitational wave, collider and dark matter signals from a scalar singlet electroweak baryogenesis, J. High Energy Phys. 08 (2017) 108.
[29] L. Marzola, A. Racioppi, and V. Vaskonen, Phase transition and gravitational wave phenomenology of scalar conformal extensions of the Standard Model, Eur. Phys. J. C **77**, 484 (2017).
[30] W. Chao, H. K. Guo, and J. Shu, Gravitational Wave Signals of Electroweak Phase Transition Triggered by Dark Matter, J. Cosmol. Astropart. Phys. 09 (2017) 009.
[31] L. Bian, H. K. Guo, and J. Shu, Gravitational waves, baryon asymmetry of the Universe and electric dipole moment in the *CP*-violating NMSSM, arXiv:1704.02488.
[32] W. Chao, W. F. Cui, H. K. Guo, and J. Shu, Gravitational Wave Imprint of New Symmetry Breaking, arXiv:1707.09759.
[33] P. S. B. Dev and A. Mazumdar, Probing the Scale of New Physics by Advanced LIGO/VIRGO, Phys. Rev. D **93**, 104001 (2016).
[34] Y. Aoki, G. Endrodi, Z. Fodor, S. D. Katz, and K. K. Szabo, The order of the quantum chromodynamics transition predicted by the standard model of particle physics, Nature (London) **443**, 675 (2006).
[35] P. Petreczky, Lattice QCD at non-zero temperature, J. Phys. G **39**, 093002 (2012).
[36] T. Bhattacharya *et al.*, QCD Phase Transition with Chiral Quarks and Physical Quark Masses, Phys. Rev. Lett. **113**, 082001 (2014).
[37] Z. Fodor and S. D. Katz, Critical point of QCD at finite T and mu, lattice results for physical quark masses, J. High Energy Phys. 04 (2004) 050.
[38] D. J. Schwarz and M. Stuke, Lepton asymmetry and the cosmic QCD transition, J. Cosmol. Astropart. Phys. 11 (2009) 025; Erratum, J. Cosmol. Astropart. Phys. 10 (2010) E01.
[39] M. Ahmadvand and K. Bitaghsir Fadafan, Gravitational waves generated from the cosmological QCD phase transition within AdS/QCD, Phys. Lett. B **772**, 747 (2017).
[40] C. Caprini, R. Durrer, and X. Siemens, Detection of gravitational waves from the QCD phase transition with pulsar timing arrays, Phys. Rev. D **82**, 063511 (2010).
[41] M. Ahmadvand and K. Bitaghsir Fadafan, The cosmic QCD phase transition with dense matter and its gravitational waves from holography, arXiv:1707.05068.
[42] M. Holthausen, J. Kubo, K. S. Lim, and M. Lindner, Electroweak and Conformal Symmetry Breaking by a Strongly Coupled Hidden Sector, J. High Energy Phys. 12 (2013) 076.
[43] Y. Ametani, M. Aoki, H. Goto, and J. Kubo, Nambu-Goldstone Dark Matter in a Scale Invariant Bright Hidden Sector, Phys. Rev. D **91**, 115007 (2015).
[44] T. Hur, D. W. Jung, P. Ko, and J. Y. Lee, Electroweak symmetry breaking and cold dark matter from strongly interacting hidden sector, Phys. Lett. B **696**, 262 (2011).
[45] T. Hur and P. Ko, Scale Invariant Extension of the Standard Model with Strongly Interacting Hidden Sector, Phys. Rev. Lett. **106**, 141802 (2011).
[46] M. Heikinheimo, A. Racioppi, M. Raidal, C. Spethmann, and K. Tuominen, Physical Naturalness and Dynamical Breaking of Classical Scale Invariance, Mod. Phys. Lett. A **29**, 1450077 (2014).
[47] J. Kubo, K. S. Lim, and M. Lindner, Gamma-ray line from Nambu-Goldstone Dark Matter in a Scale Invariant Extension of the Standard Model, J. High Energy Phys. 09 (2014) 016.
[48] H. Hatanaka, D. W. Jung, and P. Ko, AdS/QCD approach to the scale-invariant extension of the standard model with a strongly interacting hidden sector, J. High Energy Phys. 08 (2016) 094.
[49] Y. Nambu, Axial Vector Current Conservation in Weak Interactions, Phys. Rev. Lett. **4**, 380 (1960).
[50] Y. Nambu and G. Jona-Lasinio, Dynamical Model of Elementary Particles Based on an Analogy with Superconductivity. 1., Phys. Rev. **122**, 345 (1961).
[51] Y. Nambu and G. Jona-Lasinio, Dynamical Model Of Elementary Particles Based On An Analogy With Superconductivity. Ii, Phys. Rev. **124**, 246 (1961).
[52] T. Kunihiro and T. Hatsuda, A self-consistent Mean Field Approach to the Dynamical Symmetry Breaking: The effective potential of the Nambu-Jona-Lasinio model, Prog. Theor. Phys. **71**, 1332 (1984).
[53] T. Hatsuda and T. Kunihiro, QCD phenomenology based on a chiral effective Lagrangian, Phys. Rep. **247**, 221 (1994).
[54] K. Tsumura, M. Yamada, and Y. Yamaguchi, Gravitational wave from dark sector with dark pion, J. Cosmol. Astropart. Phys. 07 (2017) 044.
[55] C. Patrignani *et al.* (Particle Data Group Collaboration), Review of particle physics, Chin. Phys. C **40**, 100001 (2016).
[56] W. A. Bardeen, On naturalness in the standard model, Report No. FERMILAB-CONF-95-391-T.
[57] S. R. Coleman, The Fate of the False Vacuum. 1. Semiclassical theory, Phys. Rev. D **15**, 2929 (1977); Erratum, Phys. Rev. D **16**, 1248 (1977).
[58] C. G. Callan, Jr. and S. R. Coleman, The Fate of the False Vacuum. 2. First quantum corrections, Phys. Rev. D **16**, 1762 (1977).
[59] A. D. Linde, Decay of the False Vacuum at Finite Temperature, Nucl. Phys. **B216**, 421 (1983); Erratum, Nucl. Phys. **B223**, 544 (1983).
[60] C. L. Wainwright, CosmoTransitions: Computing Cosmological Phase Transition Temperatures and Bubble Profiles with Multiple Fields, Comput. Phys. Commun. **183**, 2006 (2012).
[61] A. Kosowsky, M. S. Turner, and R. Watkins, Gravitational radiation from colliding vacuum bubbles, Phys. Rev. D **45**, 4514 (1992).
[62] A. Kosowsky, M. S. Turner, and R. Watkins, Gravitational Waves from First Order Cosmological Phase Transitions, Phys. Rev. Lett. **69**, 2026 (1992).

[63] A. Kosowsky and M. S. Turner, Gravitational radiation from colliding vacuum bubbles: Envelope approximation to many bubble collisions, Phys. Rev. D **47**, 4372 (1993).

[64] M. Kamionkowski, A. Kosowsky, and M. S. Turner, Gravitational radiation from first order phase transitions, Phys. Rev. D **49**, 2837 (1994).

[65] C. Caprini, R. Durrer, and G. Servant, Gravitational wave generation from bubble collisions in first-order phase transitions: An analytic approach, Phys. Rev. D **77**, 124015 (2008).

[66] S. J. Huber and T. Konstandin, Gravitational Wave Production by Collisions: More bubbles, J. Cosmol. Astropart. Phys. 09 (2008) 022.

[67] M. Hindmarsh, S. J. Huber, K. Rummukainen, and D. J. Weir, Gravitational Waves from the Sound of a First Order Phase Transition, Phys. Rev. Lett. **112**, 041301 (2014).

[68] J. T. Giblin, Jr. and J. B. Mertens, Vacuum Bubbles in the Presence of a Relativistic Fluid, J. High Energy Phys. 12 (2013) 042.

[69] J. T. Giblin and J. B. Mertens, Gravitational radiation from first-order phase transitions in the presence of a fluid, Phys. Rev. D **90**, 023532 (2014).

[70] M. Hindmarsh, S. J. Huber, K. Rummukainen, and D. J. Weir, Numerical simulations of acoustically generated gravitational waves at a first order phase transition, Phys. Rev. D **92**, 123009 (2015).

[71] C. Caprini and R. Durrer, Gravitational waves from stochastic relativistic sources: Primordial turbulence and magnetic fields, Phys. Rev. D **74**, 063521 (2006).

[72] T. Kahniashvili, A. Kosowsky, G. Gogoberidze, and Y. Maravin, Detectability of gravitational Waves from Phase Transitions, Phys. Rev. D **78**, 043003 (2008).

[73] T. Kahniashvili, L. Campanelli, G. Gogoberidze, Y. Maravin, and B. Ratra, Gravitational Radiation from Primordial Helical Inverse Cascade MHD turbulence, Phys. Rev. D **78**, 123006 (2008); Erratum, Phys. Rev. D **79**, 109901 (2009).

[74] T. Kahniashvili, L. Kisslinger, and T. Stevens, Gravitational Radiation Generated by Magnetic Fields in Cosmological Phase Transitions, Phys. Rev. D **81**, 023004 (2010).

[75] D. Bodeker and G. D. Moore, Can electroweak bubble walls run away?, J. Cosmol. Astropart. Phys. 05 (2009) 009.

[76] D. Bodeker and G. D. Moore, Electroweak Bubble Wall Speed Limit, J. Cosmol. Astropart. Phys. 05 (2017) 025.

[77] J. R. Espinosa, T. Konstandin, J. M. No, and G. Servant, Energy Budget of Cosmological First-order Phase Transitions, J. Cosmol. Astropart. Phys. 06 (2010) 028.

[78] J. Kubo and M. Yamada, Genesis of electroweak and dark matter scales from a bilinear scalar condensate, Phys. Rev. D **93**, 075016 (2016).

[79] J. Kubo and M. Yamada, Scale and electroweak first-order phase transitions, Prog. Theor. Exp. Phys. **2015**, 093B01 (2015).

[80] H. Ishida, S. Matsuzaki, S. Okawa, and Y. Omura, Scale generation via dynamically induced multiple seesaw mechanisms, Phys. Rev. D **95**, 075033 (2017).

[81] N. Haba and T. Yamada, Strong dynamics in a classically scale invariant extension of the standard model with a flat potential, Phys. Rev. D **95**, 115016 (2017).

[82] R. Jinno, S. Lee, H. Seong, and M. Takimoto, Gravitational waves from first-order phase transitions: Towards model separation by bubble nucleation rate, arXiv:1708.01253.